



LAWRENCE  
LIVERMORE  
NATIONAL  
LABORATORY

# Phase transitions in Zr at sub-nanosecond time scales

P. Grivickas, R. A. Austin, M. R. Armstrong, H. B.  
Radousky, J. L. Belof

November 13, 2021

Journal of Applied Physics

## **Disclaimer**

---

This document was prepared as an account of work sponsored by an agency of the United States government. Neither the United States government nor Lawrence Livermore National Security, LLC, nor any of their employees makes any warranty, expressed or implied, or assumes any legal liability or responsibility for the accuracy, completeness, or usefulness of any information, apparatus, product, or process disclosed, or represents that its use would not infringe privately owned rights. Reference herein to any specific commercial product, process, or service by trade name, trademark, manufacturer, or otherwise does not necessarily constitute or imply its endorsement, recommendation, or favoring by the United States government or Lawrence Livermore National Security, LLC. The views and opinions of authors expressed herein do not necessarily state or reflect those of the United States government or Lawrence Livermore National Security, LLC, and shall not be used for advertising or product endorsement purposes.

# Phase transitions in Zr at sub-nanosecond time scales

---

P. Grivickas\*, R. A. Austin, M. R. Armstrong, H. B. Radousky, and J. L. Belof

Lawrence Livermore National Laboratory, 7000 East Ave., Livermore, California 94551, USA

---

## Abstract

Solid-solid phase transitions are investigated in Zr thin films using shock compression induced by a short laser pulse ( $< 1$  ns). Shock wave profiles are measured at free surfaces for films of different thicknesses (a few micrometers) using chirped pulse line velocimetry with 10 ps time resolution. Experiments are performed at pressures up to  $\sim 50$  GPa, which is sufficient to reach the  $\omega$  and  $\beta$  phases. The shock wave structures are analyzed using a general Lagrangian analysis method, which allows for the calculation of stress-strain paths and assessments of phase transition behavior. In agreement with recent short laser pulse experiments using ultra-fast x-ray diffraction, we do not find any clear evidence of the  $\alpha$ - $\omega$  transition, though this would be expected from the phase diagram. Instead, we infer a direct transformation to a metastable  $\beta$ -phase at lower shock pressures ( $< 20$  GPa) and equilibrium  $\beta$  at higher pressures. Through the velocimetry analysis, we find  $\alpha$ - $\beta$  transformation onset times of less than  $\sim 100$  ps and completion times of less than  $\sim 200$  ps.

\* Email of corresponding author: grivickas1@llnl.gov

## Introduction

Under quasi-static deformation, phase transformations in a material are mostly controlled by thermodynamic conditions induced by a specific loading path. Under dynamic deformation, transformations are further influenced by the kinetics of transformation mechanisms. One way to study such effects are impact experiments at gun facilities, which involve observed strain rates as high as  $10^8/s$ . Manifestation of a specific phase transformation in an impacted material is commonly inferred from the observed shock wave structure. It has been shown that at higher rates ( $> 10^8/s$ ) phase transformation parameters (such as relaxation time and threshold pressure) can differ significantly from those observed in gas gun experiments. For example, when the  $\alpha$ - $\epsilon$  transition in Fe was induced in laser-driven shock compression experiments (at  $\sim 10^{10}/s$ ) the observed transformation completion times were orders of magnitude faster and the transformation stress was roughly twice as large in comparison to gas gun results at lower rates<sup>1</sup>.

With increasing pressure along the shock Hugoniot, Zr is known to exhibit the following sequence of solid phases:  $\alpha$  (hexagonal close packed),  $\omega$  (hexagonal close packed), and  $\beta$  (body-centered cubic). The multi-phase equation of state (EOS) of Greeff et al.<sup>2</sup> reflects these shock transitions and, more generally, the Zr phase diagram over a range of pressure and temperature. The role of kinetic effects on Zr solid-solid transformations has been investigated previously using both shock and ramp wave loading in impact experiments.<sup>3-8</sup> The  $\alpha$ - $\omega$  transition has been detected at  $\sim 8$  GPa, but the exact pressure of this transition depends strongly on impurity content<sup>3,4</sup>. The  $\omega$ - $\beta$  transition has been detected at  $\sim 27$  GPa, but the clear transition signatures were only present in the velocimetry data for long ( $> 100$  ns) ramp waves<sup>4</sup> or in sound speed measurements using the front surface impact approach<sup>9</sup> with no clear dependency on impurity content<sup>4</sup>.

The possibility of different atomic-level transformation mechanisms has been predicted for Zr at very high strain rates<sup>1,10-12</sup>. Indeed, during laser compression it was observed that transition to the  $\omega$  phase is inhibited on a sub-nanosecond time scale, while transition to  $\beta$  occurs at very short ( $< 100$  ps) time scales.<sup>6-8</sup> These conclusions were derived solely from x-ray diffraction data obtained at synchrotron facilities. In this work, we examine laser generated shocks using ultrafast velocimetry measurements. Experiments are performed in sputtered polycrystalline Zr films of different thicknesses to probe wave structure evolution. The wave profiles are analyzed using a general Lagrangian analysis method<sup>13,14</sup>, which provides quantitative information about stress-volume paths and the timing of phase transitions in dynamically compressed Zr.

## Experiments

Schematics of the laser shock compression experiments, which involve stepped targets of various thickness and laser energies of 0.5 and 2.0 mJ, are shown in Figure 1. The approach adopted here is nearly identical to previous studies using the same ultrafast system<sup>1,10,11</sup>. Zr was deposited on a glass coverslip pre-coated with 140 nm of Al. Shock waves were generated by focusing a laser beam onto the Al layer through the glass cover slip, the latter acting as an ablation tamper (see Figure 1(a)). A stress impulse launched in the Al layer propagated into the Zr film and was detected on the Zr free-surface using chirped-pulse line velocimetry. The temporal resolution of this system is tens of picoseconds, as demonstrated in previous work<sup>15</sup>. Examples of the damage left on the Zr film drive surface from individual shots are shown in Figure 1(b). The symmetrical appearance of the damage field is consistent with the Gaussian profile of the drive pulse. The size of the spectrometer slit (used for velocity measurement) relative to the drive laser spot size is illustrated in Figure 1(c). The one-dimensional shock profiles discussed below refer to the peak of the Gaussian laser

intensity distribution. The temporal profile of the averaged laser pulse is shown in Figure 1(d).

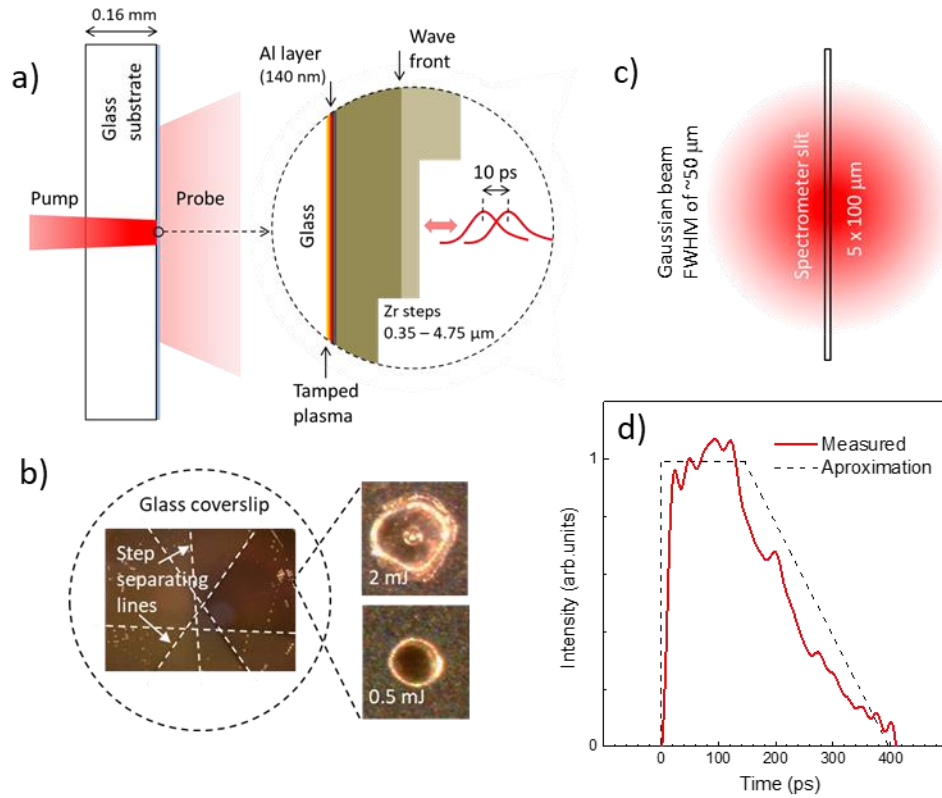


**Figure 1:** a) Schematics of laser shock compression experiments in stepped Zr targets; b) photograph of the sample surface showing examples of craters generated by the drive laser; c) region of the velocimetry probe (spectrometer slit) with respect to spatial distribution of the drive laser; d) temporal profile of the drive laser.

Zr films with several steps (of different thickness) were deposited on a single coverslip using shadowing masks, with the step separation lines from the shadowing masks shown in Figure 1(b). In total, six steps were deposited with final average thicknesses of 0.35, 0.82, 1.34, 2.25, 3.80, and 4.75 μm. The cited thicknesses exclude the 140-nm thick Al layer, which largely transforms into plasma during the drive pulse. Thickness measurements were performed using optical profilometry (Zygo instrument) at the damage craters where the surface of the glass coverslip was partially exposed. The standard uncertainty of these measurements was estimated to be +/- 40 nm for all layers. In addition, the thickest layer was

cross-sectioned using a focused ion beam and examined using scanning electron microscopy (SEM) as shown in Figure 2(a). The arrows in the image indicate interruptions of the columnar growth occurring during the mask relocation process. The relative thickness of these regions provided a mean of estimating the total thickness for each step. The values obtained this way were within the uncertainties established by the optical profilometry.

The area labeled “1” in Figure 2(a) was selected for microstructure and texture analysis using a transmission electron microscope (TEM). Figure 2(b) shows the bright field TEM image of this area, which indicates columnar growth of grains reaching an average diameter of 100 to 200 nm. The diffraction data collected from the TEM is summarized in the pole plot of Figure 2(b) with the color coding represented in the units of multiples of a random distribution (MRD). The result shows preferred crystallographic orientation in the layers being along the 0001 axes and coinciding with the growth direction (y-axis on the plot).

The area labeled “2” in Figure 2(a) was selected for composition analysis using energy-dispersive x-ray spectroscopy. Figure 2(c) shows a magnified image of this area with the location of the x-ray scan indicated by the white dash. In Figure 2(c), the plot to the right of the image tracks the content of Zr, C and O along the scan, showing the expected surface oxidation at the growth interruption boundary. The full energy spectra in the beginning of the scan (labeled as “middle”) and at the boundary are shown at the bottom of Figure 2(c); they indicate presence of Hf in Zr layers (C and Ga signals are mostly artifacts). Hf content was independently quantified using Rutherford backscattering spectrometry (RBS). The obtained Hf amount of 4% by weight agrees with the 4.5% maximum value allowed for the grade 702 Zr used as a target in the sputtering process (obtained from Kurt. J. Lesker Co.).

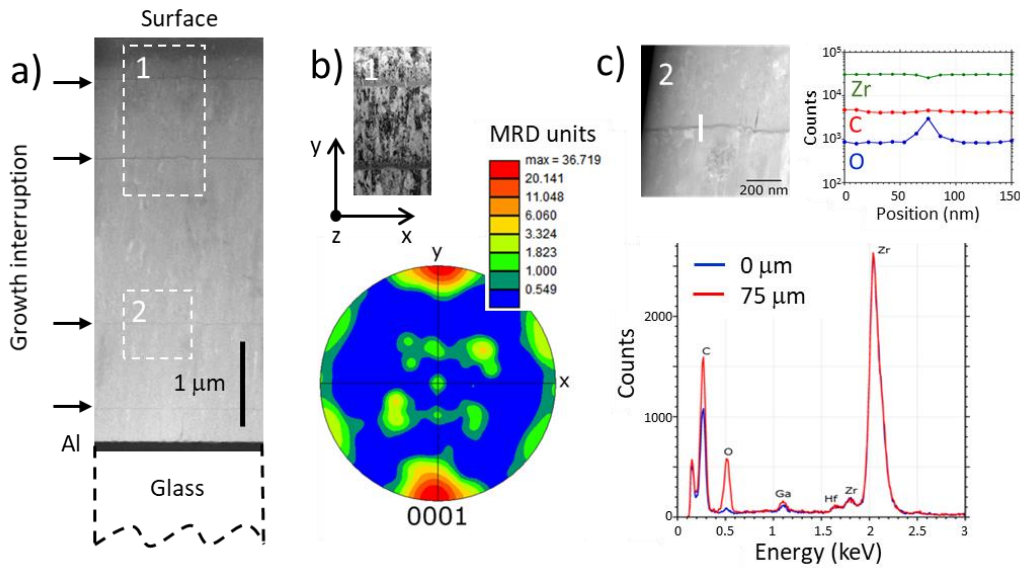


**Figure 2: Sample characterization: a) SEM image of the sample cross-section for the step thickness of 4.95  $\mu\text{m}$  with the side arrows indicating interruptions during growth; b) TEM image of the area “1” as indicated in a) (same scale) showing the structure of columnar Zr grains; crystallographic orientation of the grains in the area is summarized in the polar plot; c) enlarged image of the area “2” as indicated in a) showing the path of x-ray spectroscopy scan at a re-growth interface (white line); the full chemical composition obtained at the two scan positions is shown on the bottom while the relative changes of Zr, C and O along the scan are shown on the right.**

## Results

### 1. Experimental observations

Velocimetry data obtained from the six Zr steps at two laser energies are summarized in Figure 3. The top row shows the two-dimensional (2D) line velocimetry results in full for each step. They were obtained by averaging of up to 5 individual shots and applying spatial filtering to remove high frequency noise.<sup>15</sup> All individual shots within each average had virtually the same arrival time and the same shock rise profile, whereas at later times individual profiles exhibited modest variations in velocity ( $< 10\%$ ), in agreement with previous reports on laser shock compression experiments.<sup>1,10,11</sup> In the spatial coordinate, all velocity profiles in Figure 3 are symmetric with respect to the midpoint, with velocity tapering towards the edges as expected for the Gaussian drive pulse. The one-dimensional (1D) time histories of free-surface velocity were extracted at the midpoints and plotted together for all the steps in the bottom row of the Figure 3. At 0.5 mJ, the wave profile for the

thinnest  $0.35\ \mu\text{m}$  layer exhibits two jumps in velocity. The first wave, with an amplitude of  $\sim 2\ \text{km/s}$ , is observed for thicker samples (which develop precursor wave structure), whereas the second jump is no longer present. At  $2.0\ \text{mJ}$ , the wave profile for the thinnest  $0.35\ \mu\text{m}$  layer is qualitatively similar, but the first wave has an overshoot feature and exhibits amplitude decay with increasing sample thickness.

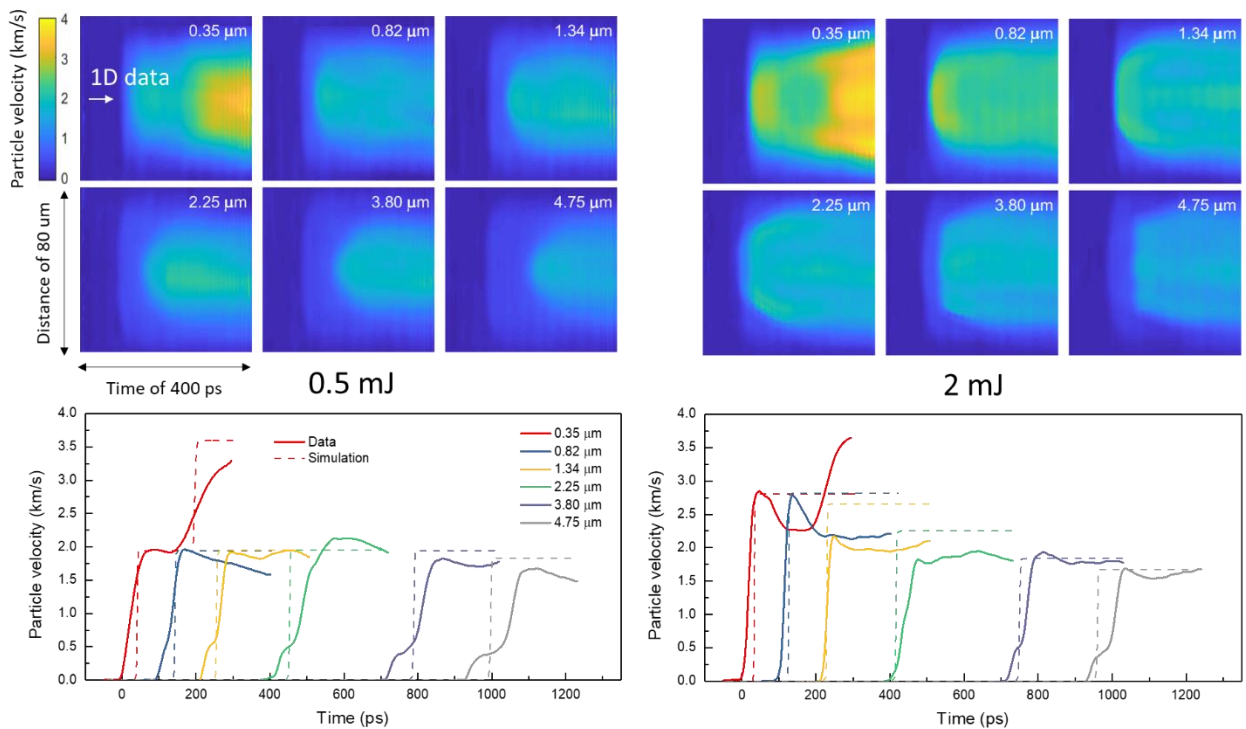


**Figure 3: (top) 2D free-surface velocity data for each sample thickness. The vertical axis is the spatial position along the spectrometer slit and the horizontal axis is time. (bottom) 1D velocity data (solid curves) at each Zr step thicknesses taken from the center position in the 2D plots. Dashed curves show results from hydrodynamic simulations. Data on the left/right corresponds to the drive pulse energy of 0.5/2.0 mJ, respectively.**

## 2. Hydrodynamic simulation

The laser shock compression experiments were simulated using a hydrocode to help understand the wave dynamics in the Zr layers. The simulations were useful for assessing the arrival times of various features, wave interactions, and pressure decay with run distance, which stems from the short drive pulse. The mechanical response of the Zr layers was

modeled using a Gruneisen EOS based on the principal Hugoniot<sup>16</sup> as described previously<sup>6</sup>. This model does not account for material strength (deviatoric response) or any solid-solid phase transformations.

The simulations assume the Al layer is fully ablated, producing a pressure pulse on the front face of the Zr layer. The time-dependence of the pressure pulse was approximated using the laser intensity profile, as shown in Figure 1(d). The peak pressure, the peak-pressure hold time, and the pressure release time were then tuned to agree with the measured free-surface velocities. Simulation results for selected Zr thicknesses are plotted in Figure 4 as pressure fields in the Lagrangian space-time plane for the two laser energies. The material model employed here does not account for mechanical strength (deviatoric stress) or resistance to volumetric expansion (negative pressure). Therefore, the overlap of release waves from the drive- and free-surfaces will induce material separation along an internal plane (spallation) with zero resistance. Accordingly, the model will not reproduce velocimetric pull-back signatures from the peak compression state, should they be detected. Simulation results beyond spallation events should be interpreted in the context of this simple treatment.

The results for the 0.5 mJ energy are shown on the top row of Figure 4. For the 0.35- $\mu\text{m}$  case, the Zr target is sufficiently thin for the first release wave from the free surface to arrive back at the drive surface before the drive loading profile is complete. This results in a second compressive pulse that propagates through the unloaded Zr layer. The second pulse produces a second jump in particle velocity at the free surface. This second jump is indeed recorded in the experimental profile (see Figure 3). In thicker samples (1.34 and 3.80  $\mu\text{m}$ ), the second pulse is absent and typical behavior is observed, with release waves from the drive surface catching up to the main compression wave. However, the release waves do not reach the leading shock before breakout occurs at the free surface. At 2.0 mJ (bottom row of Figure 4), the thinnest sample (0.35  $\mu\text{m}$ ) does not exhibit the second compressive pulse because the

rarefaction fan from the free surface coincides with the end of the drive profile. In the thicker samples (1.34 and 3.80  $\mu\text{m}$ ), the leading shocks decay as they approach the free surface due to catch-up of release waves from the drive surface.

The simulated free-surface velocity profiles are plotted in Figure 3 (dashed curves) for all target thicknesses, in comparison to the measurements. In general, we find good agreement in amplitudes and timing, while several deviations in structure can be explained in terms of modeling assumptions/simplifications. For example, slight errors in the assumed pressure drive profiles are most likely responsible for the differences at 2.0 mJ (i.e., the absence of a second jump in the simulated free-surface velocity and the less-pronounced decay of simulated amplitudes at intermediate thicknesses). In addition, the precursor wave structure (observed in many of the experimental profiles) is a strength effect and the structure of the main/plastic wave depends on the kinetics of deformation and/or any solid-solid phase transitions, should they occur. The hydrodynamic model does not account for any of this behavior. In the next section, we analyze these wave structures to assess the onset and progress of solid-solid phase transitions.

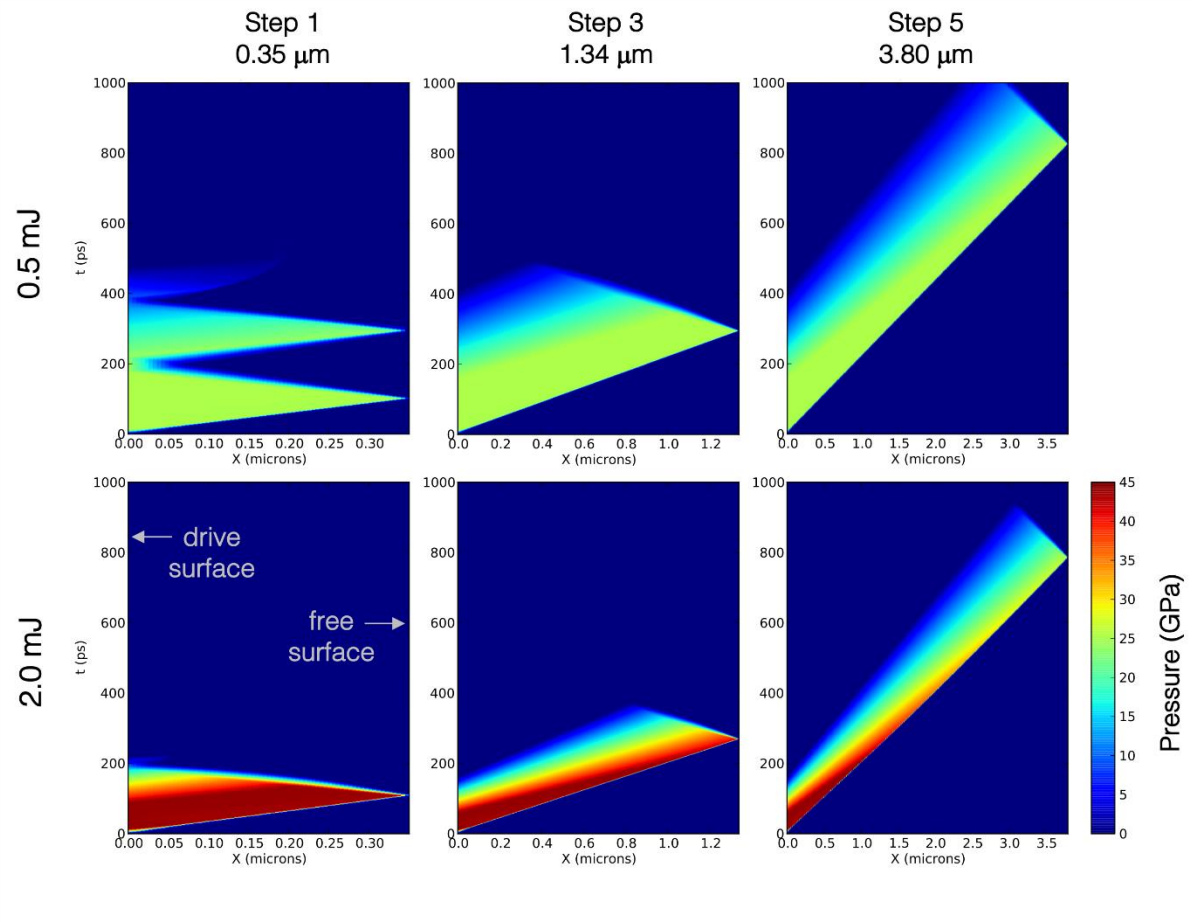


**Figure 4: Pressure fields obtained by hydrodynamic simulation of selected target thicknesses (0.35, 1.34, and 3.80  $\mu\text{m}$ ) for the two drive energies of 0.5 and 2.0 mJ. The spatial coordinate ( $X$ ) denotes the Lagrangian position within the Zr layer. The pressure drive is applied at  $X=0$  and free surfaces are located on the right-hand side.**

### 3. Lagrangian analysis

The measurements of free-surface velocity (Figure 3) are analyzed using a Lagrangian method that was developed in previous work<sup>13,14,17</sup>. Here, the measurements at a given energy are used to reconstruct the *in-situ* velocity field and compute the stress-strain paths of Lagrangian volume elements in a semi-infinite medium. The stress-strain trajectories are then analyzed to infer aspects of elastic/plastic response and the onset and progress of solid-solid phase transitions.

The analysis method assumes: (i) all waves are one-dimensional and symmetric under rotations about the direction of propagation; (ii) the waves involve uniaxial strain; and (iii) the measurements sample the same compression wave at different propagation distances. The method does not assume the measured wave forms are steady (i.e., one form that propagates at constant speed) or simple (i.e., one form that is simply rescaled in space/time). Therefore, it can handle evolving wave forms with time-dependent material behavior without invoking further simplifying assumptions. A brief description of the Lagrangian analysis method is given in the following; previous work<sup>13,14,17</sup> should be referenced for further details.

The measurements of free-surface velocity,  $u_m(t)$ , from each target thickness (or step height),  $h_i$ , are used to reconstruct the *in-situ* particle velocity field,  $u(X, t)$ , over a patch of Lagrangian space-time. To obtain estimates of *in-situ* particle velocity, the effects of the free surface need to be removed. This is achieved by applying simple corrections to the measured profiles, which account for differences in shock impedance (velocity doubling at the free surface) and precursor waves that reflect from the free surface and interact with the trailing compression wave. Bicubic splines are fit to the *in-situ* velocity profiles, which allows for interpolation/extrapolation of the velocity field in space and time. From the inferred *in-situ* particle velocity field, the stress and strain are obtained by integrating the conservation equations, i.e.,

$$\frac{\partial \epsilon}{\partial t} = -\frac{\partial u}{\partial X} \quad (1)$$

$$\frac{\partial \sigma}{\partial X} = -\rho_0 \frac{\partial u}{\partial t} \quad (2)$$

where  $\epsilon = 1 - V/V_0$  is the axial strain,  $V/V_0$  is the relative volume,  $\sigma$  is the axial Cauchy stress, and  $\rho_0$  is the reference density. Here, we note (i) the axial components of the nominal stress (reference frame) and Cauchy stress (current frame) are identical under uniaxial strain, and (ii) the above measures of stress and strain are positive under compression. For materials

that do not undergo phase transitions, it is possible to extract strength information (deviatoric response) by identifying an equation of state for the volumetric response and a shear modulus. As this study focuses on solid-solid phase transitions, we do not attempt to extract strength information and therefore do not assume any other properties or constitutive relations. For our purposes, the experimental velocity profiles and the reference density of  $\alpha$ -Zr ( $\rho_0 = 6.506$  g/cm<sup>3</sup>) are sufficient to compute stress-strain trajectories.

The analysis of data taken at 0.5 mJ is shown in Figure 5. For convenience, the analysis considers steps 1-3 and steps 4-6 as independent sets at each drive energy. This approach was adopted to simplify the sample thickness calibration scheme (discussed below) and to avoid certain non-monotonic features of wave structure evolution (see, for example, the peak amplitudes measured at step 4). We have verified that nearly equivalent results are obtained by considering all steps (1-6) as a single set. Plotted in Figure 5 (top row) are the experimentally-measured and corrected velocity for each thickness (solid curves), the corresponding spline fits (dotted curves, which nearly overlay the data), and the spline knots (open circles). In some cases, the knots correspond to physically-meaningful wave features; in other cases, they are merely convenient choices for the fitting algorithm. As shown in Figure 5, the analysis follows the compression response from wave arrival (blue circles) to peak compression (cyan circles) at each step. Fitting knots were also attached to elastic precursors (green circles) and points roughly half-way through the main compressive wave (red circles). The velocity profiles at other positions (light gray curves), which are needed for integration purposes, are obtained by interpolation or extrapolation of the fitted velocity function,  $u(X, t)$ . Here, we note that extrapolated profiles only factor into the stress evaluation at the last step in each set. At steps 3 and 6, extrapolated velocity profiles are only needed for time windows that span wave arrival (blue circles) and peak compression (cyan circles). Therefore, the oscillatory features that appear at later times do not factor into our calculations.

For reference, we plot in Figure 5 (bottom row) the Hugoniot pressure curves of the  $\alpha$ ,  $\omega$ , and  $\beta$  phases (including metastable extensions) as derived from the Greeff EOS<sup>2</sup>. Also plotted here is the  $\alpha$ -phase elastic isentrope under uniaxial strain, which serves as good approximation of the elastic Hugoniot. The elastic isentrope is computed as  $\sigma_s = p_s - \frac{4}{3}\mu(p_s) \ln(V/V_0)$ , where the isentropic pressure,  $p_s$ , comes from the EOS and the shear modulus is taken as  $\mu(p) = \mu_0 + \mu'_0 p$ , with  $\mu_0 = 36.0$  GPa and  $\mu'_0 = 1.368$ .<sup>16</sup> We reiterate that the EOS and shear modulus are used to help interpret the results; they are not required to carry out the stress/strain integration.

Our initial attempt to compute stress-strain trajectories from the reconstructed velocity fields,  $u(X, t)$ , yielded results that were clearly in error. For example, during the compression of the elastic precursor wave, the computed stress deviated significantly from the elastic compression curve; and terminal points (corresponding to peak particle velocity) landed far from the Hugoniot curves. Analysis revealed that ps-level errors in timing and/or nm-level errors in sample thickness can account for these deviations. To address these errors, we adjusted the Zr sample thicknesses by small amounts to calibrate the initial segment of the stress-strain trajectory at each step to fall along the elastic compression curve – a reasonable assumption given the presence of elastic precursor waves. This amounted to thickness adjustments of <35 nm for steps 1-3 and <15 nm for steps 4-6, which are within the uncertainty of measurements obtained using the Zygo instrument (+/- 40 nm). Although timing errors might also contribute to stress-strain trajectory errors, the timing errors are thought to be, at most, ~1 ps. Since trajectory uncertainty from thickness and timing errors manifest in approximately the same way, timing corrections on the order of ~1 ps translate to thickness corrections of only ~5 nm. As such, we do not attempt to distinguish timing errors here.

With sample thicknesses calibrated to reproduce the initial elastic response, the stress/strain integration yielded the results given in Figure 5 for the 0.5 mJ data. In these plots, there is a correspondence between the open circles of the velocity-time profiles and the stress-volume profiles. All terminal points now fall near the  $\beta$ -phase Hugoniot.

The same procedure was followed for analyzing the 2.0 mJ data (see Figure 6). Again, the samples were grouped into two sets (steps 1-3 and 4-6) and thickness adjustments of  $<35$  nm (for steps 1-3) and  $<20$  nm (for steps 4-6) were employed to calibrate the initial parts of stress-volume paths to the elastic compression curve. Again, at steps 3 and 6, extrapolated velocity profiles are only needed for limited time windows (as above) so that oscillations at later times are excluded. In this case, we note the elastic precursor amplitude at step 4 is somewhat higher than those of the surrounding steps, which can pose a challenge to the fitting algorithm if all steps (1-6) are considered as a single set. We do not attempt to remedy this peculiarity; rather, we analyze the data as they are. As shown in Figure 6, the terminal points for most all stress-volume trajectories fall near the  $\beta$ -phase Hugoniot.

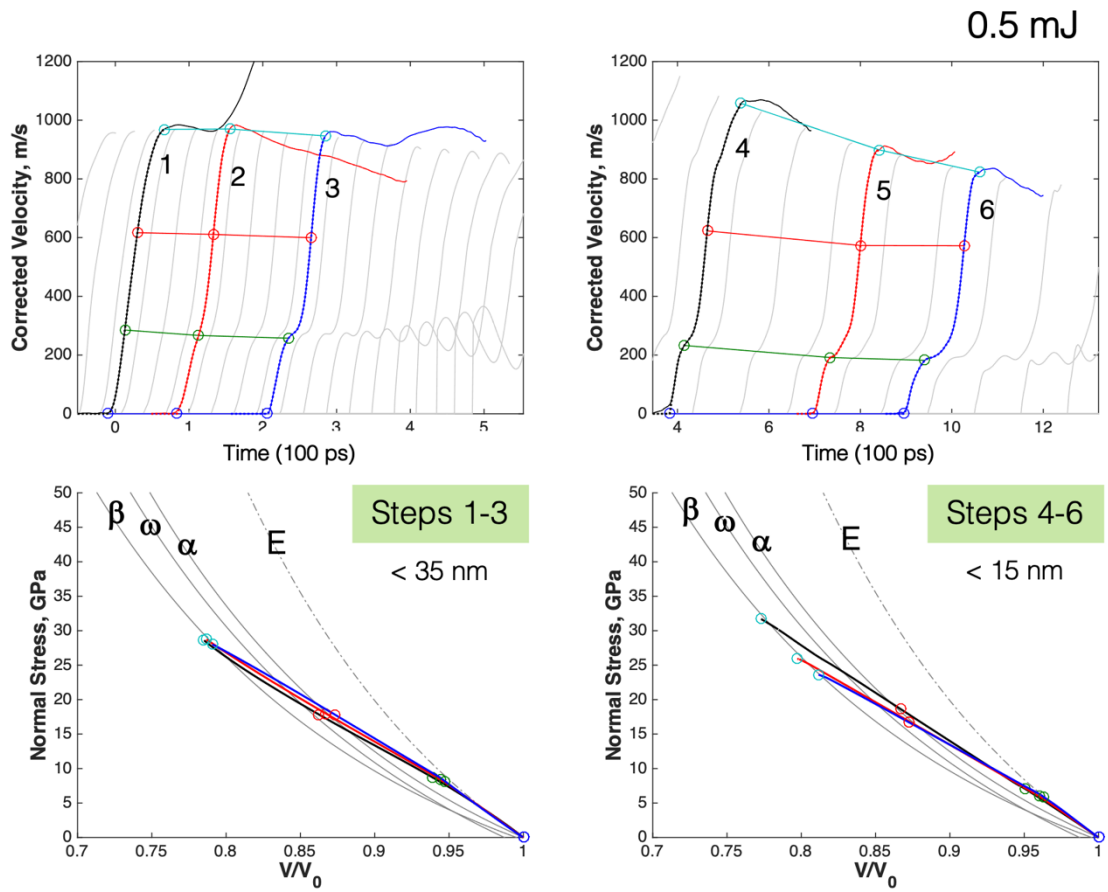


**Figure 5: Results from Lagrangian analysis of the 0.5 mJ data.** The top panels show the corrected *in-situ* velocity at steps 1-3 and 4-6 (solid curves), the spline fits (dotted curves), the spline knots (open circles), and the velocity profiles for other cuts through the space-time plane (light gray curves). The bottom row shows the stress-volume paths obtained by integration at the corresponding steps, the Hugoniot curves for the  $\alpha$ ,  $\omega$ , and  $\beta$  phases, and the  $\alpha$ -phase elastic isentrope under uniaxial strain (E). The maximum thickness adjustment for each data set is indicated.

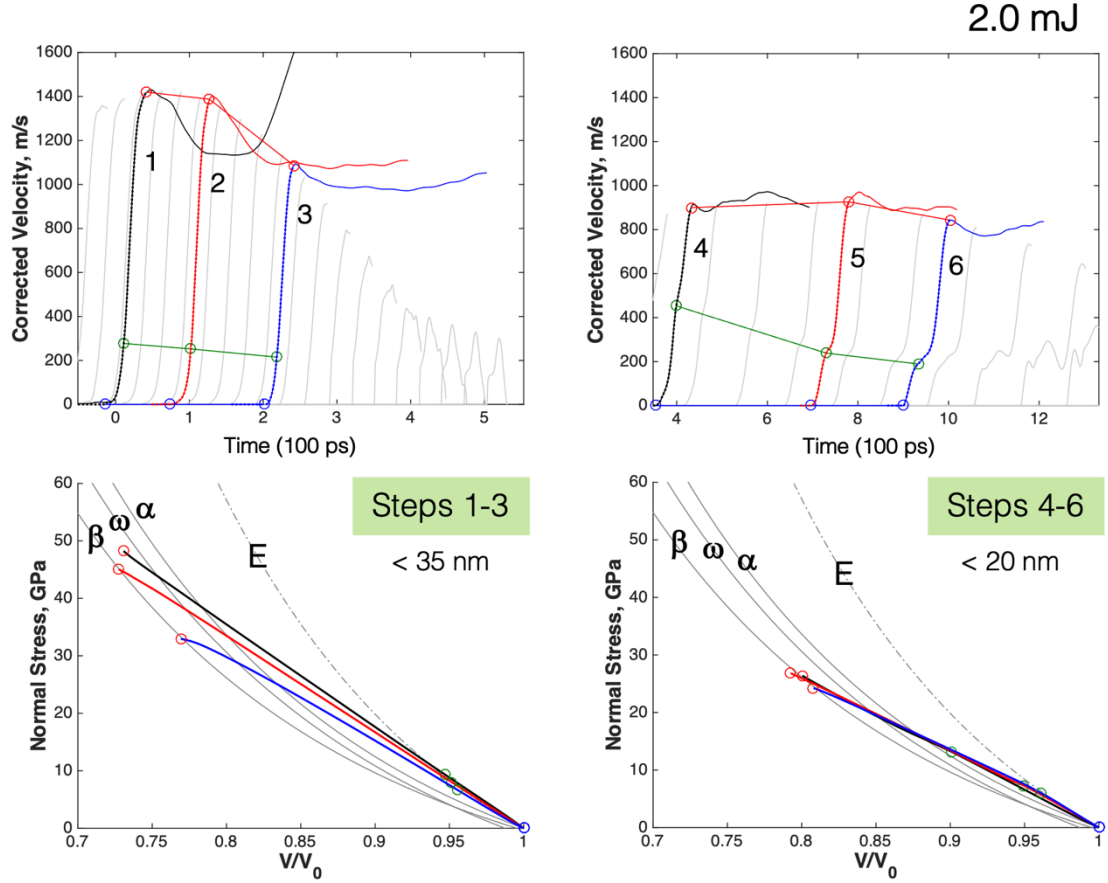


**Figure 6: Results from Lagrangian analysis of the 2.0 mJ data.** The top panels show the corrected *in-situ* velocity at steps 1-3 and 4-6 (solid curves), the spline fits (dotted curves), the spline knots (open circles), and the velocity profiles for other cuts through the space-time plane (light gray curves). The bottom row shows the stress-volume paths obtained by integration at the corresponding steps, the Hugoniot curves for the  $\alpha$ ,  $\omega$ , and  $\beta$  phases, and the  $\alpha$ -phase elastic isentrope under uniaxial strain (E). The maximum thickness adjustment for each data set is indicated.

#### 4. Uncertainty quantification

Several factors contribute to uncertainty in the computed stress-volume paths. For example, uncertainties in analysis inputs such as target thickness, the time origin of loading for each step, measured free-surface velocity, and the placement of spline knots in the velocity fitting scheme. The uncertainty in the computed stress-volume paths was calculated by propagating these uncertainties through the numerical analysis using a linearized sensitivity matrix.

The overall uncertainty in stress-volume response is dominated by the uncertainty in step thicknesses. Considering the experimental thickness uncertainty of  $\pm 40$  nm, we derive the uncertainty bounds shown in Figure 7. Here, we note the nominal stress-volume paths (solid curves in Figure 7) are for the as-calibrated thickness values rather than the raw measurements. Therefore, an uncertainty of  $\pm 40$  nm (relative to calibrated values) represents a conservative estimate of errors. Other sources of error were considered, i.e., particle velocity measurement (VISAR) uncertainties of 2%, and variations in the spline knots of  $\pm 5$  ps. However, the errors associated with these inputs were found to be small relative to errors from thickness uncertainty.

For steps 1 and 3 at both energies (Figure 7(a) and (c)), the uncertainty bounds in stress-volume response are considerably larger than those at step 2. This is expected because the intermediate step (a non-edge case) recovers the most accurate spatial derivatives of particle velocity and does not employ any extrapolation for well-chosen step heights. As such, the results from an intermediate step are often viewed as being the most reliable<sup>13,14</sup>. Although the stress-volume uncertainty bounds are rather large at steps 1 and 3, recall that an uncertainty estimate of  $\pm 40$  nm is conservative for the calibrated thickness values. For steps 4-6 at both energies (Figure 7(b) and (d)), the error bounds are relatively narrow, which provides confidence in our inference of Zr response. Again, the results at step 5 are viewed as the most reliable. As expected, the stress-volume uncertainty bounds are narrower at steps 4-6 because the fractional thickness uncertainty is smaller.

The analysis results presented here highlight the need for high levels of precision in experimental timing and sample metrology. In previous work<sup>14,17</sup>, which involved gas-gun compression of Ta targets (1-2 mm in thickness), analysis errors were dominated by timing uncertainties of  $\sim 1$  ns, whereas the uncertainties derived from target thickness variation ( $\sim 1$   $\mu\text{m}$ ) were small in comparison. In the work at hand, the experiments achieve exceptional time

resolution ( $\sim 10$  ps) but the thin size of the Zr layers allows for nm-scale variation/uncertainty to dominate errors in the inferred stress-volume paths. Although a thickness uncertainty of 40 nm is relatively small in an absolute sense, it comprises approximately 1 to 10 percent of the Zr target thicknesses considered here.

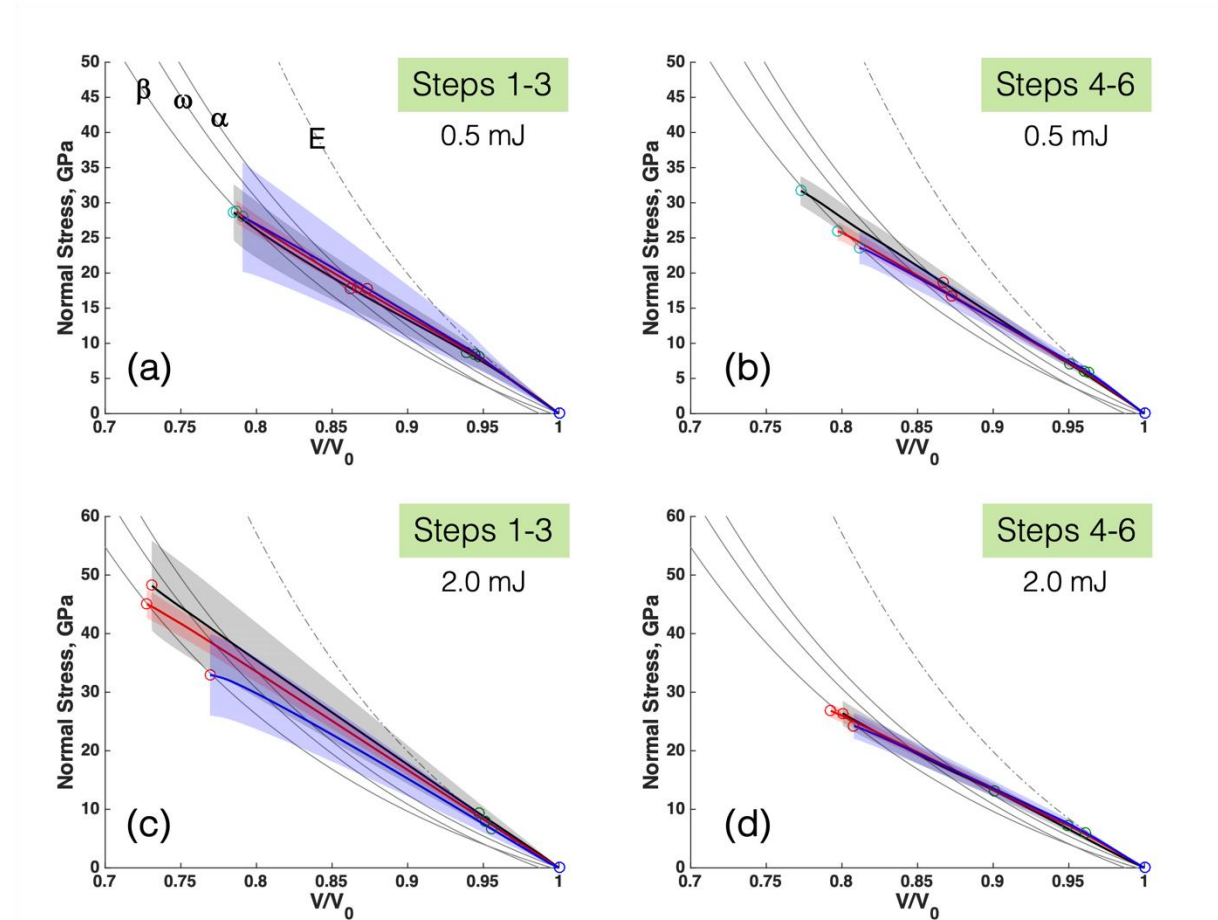


**Figure 7:** Uncertainty bounds plotted as shaded regions for the stress-volume paths at 0.5 mJ (a, b) and 2.0 mJ (c, d). These bounds consider a sample thickness uncertainty of  $\pm 40$  nm. The curve colors for steps 1-3 and 4-6 are, respectively, black, red, and blue.

## Discussion

The analysis of the 0.5 mJ shots is shown in Figure 5. At *in-situ* Lagrangian positions equivalent to the step heights, the stress-volume paths follow the elastic compression curve

(per the calibration scheme) and then relax towards a stress state on the  $\beta$ -phase Hugoniot.

The Hugoniot curves drawn in Figure 5 indicate the shock pressure of each phase at a given level of compression (including metastable extensions). Since they are derived from an analytical EOS, they do not include the any strength (deviatoric) contributions. Relaxation over the loading path occurs by plastic deformation and/or phase transformation. Although we cannot apportion the relative contributions of these mechanisms, we can make some inferences pertaining to the onset and progress of phase transformations.

If a given phase is shock-compressed to a certain stress level, the stress-volume path should never pass through the Hugoniot curve (of that phase) to a point of higher compression. Therefore, if a stress-volume trajectory passes through a Hugoniot curve, we may infer that a phase transition is occurring. As phase fractions evolve, the actual Hugoniot curve shifts among the pure phases and the material relaxes toward the corresponding state.

In previous work<sup>1</sup>, the  $\alpha$ - $\epsilon$  transition in Fe was identified by the apparent onset of strongly negative plastic dissipation during compression. Since this would appear to violate the second law of thermodynamics, its occurrence was associated with some physical process not considered in the analysis, i.e., phase transformation. The negative dissipation criterion for phase transformation is largely consistent with the Hugoniot intersection criterion discussed above. This stems from the relationship among the axial stress, pressure, and maximum shear stress in an isotropic medium, i.e.,  $\sigma = p + \frac{4}{3}\tau$ . At a given volume, if the axial stress is less than the isentropic pressure ( $\sigma < p_s$ ), then  $\tau < 0$  and plastic strains of positive sign will produce negative dissipation. Therefore, a stress-volume path that crosses the isentrope of a given phase implies the onset of negative dissipative work within that phase. Since the principal Hugoniot serves as a reasonable approximation of the principal isentrope for the pressures considered here, a path that crosses the Hugoniot is also consistent with negative dissipation and, therefore, the onset of phase transformation. We've verified

that bulk isentropes for the  $\alpha$ ,  $\omega$ , and  $\beta$  phases fall reasonably close to the Hugoniot curves plotted in Figure 5 and that considering load path intersections of the isentropes yield essentially the same results. We've opted to plot the Hugoniot curves because the positioning of terminal states relative to the Hugoniot provides an indication of Zr phase in the shock-compressed state.

For the 0.5 mJ data (Figure 5), the stress-volume paths for steps 1-3 are similar, with all terminal points falling close to the  $\beta$ -Zr Hugoniot at  $\sim 29$  GPa. The stress-volume paths intersect the  $\alpha$ -Zr Hugoniot at stresses ranging from 15 to 20 GPa. From the time profiles, this indicates that transformation from the  $\alpha$ -phase begins in  $<60$  ps from the wave arrival time. This represents a conservative estimate for the onset of transformation, as it may start to occur before the trajectory intersects the Hugoniot. Once the path crosses the  $\alpha$ -Zr Hugoniot, the analysis indicates the material element is no longer pure  $\alpha$ -phase. That is, the element contains some amount of  $\omega$  or  $\beta$ , potentially mixed with  $\alpha$ .

The results derived from the 0.5 mJ data at steps 4-6 indicate similar behavior. Here, the stress-volume paths cross the  $\alpha$ -Zr Hugoniot at 15 to 20 GPa, which corresponds to a transformation onset time of  $<130$  ps. The onset time is expected to be longer here (as compared to steps 1-3) due to wave dispersion with run distance. We note the computed peak stress at step 4 is higher than the other steps, which is consistent with the higher observed particle velocity at that step. At steps 4-6, the peak stress decays with run distance, which is to be expected for a short-pulse drive where release waves can catch up to the leading compression wave. Indeed, forward simulations of the drive indicate wave attenuation at these step heights (see Figure 3). Again, all terminal states fall near the  $\beta$ -Zr Hugoniot, even as the wave amplitude decays.

For the 0.5 mJ shots, we provide in Table 1 the peak stresses at each step, the stress at which the  $\alpha$ -Zr Hugoniot is crossed and estimates of the transformation onset and completion

times. The Hugoniot-crossing stress provides an estimate of the transformation onset stress. The transformation onset time is the difference between the Hugoniot-crossing time and the wave arrival time. As mentioned above, the transformation onset time and stress are conservative estimates (as the transformation may begin earlier) and the onset time will naturally become larger with run distance due to wave dispersion. Since each step experiences a different loading path, it is difficult to compare transformation onset times among the steps on a one-to-one basis. The transformation completion time is taken as that required to compress an element from ambient to a point on the  $\beta$ -Zr Hugoniot curve. Again, this serves as an upper-bound because it is difficult to pin down the onset time. It is not clear if the  $\omega$ -phase is produced during the transformation from  $\alpha$  to  $\beta$ , but we do not find any clear evidence that suggests so.

The analysis of the 2.0 mJ data (Figure 6) suggests responses that are qualitatively similar to the 0.5 mJ data. At step 1, the peak stress is  $\sim 48$  GPa and the terminal state falls in-between the  $\omega$ - and  $\beta$ -Zr Hugoniot curves. At step 2, high stress persists, but the stress-volume path now terminates on the  $\beta$ -Zr Hugoniot. At step 3, the peak stress has been reduced, but the terminal state again falls on the  $\beta$ -Zr Hugoniot. The velocity profiles indicate an overshoot at steps 1 and 2, which is relieved at step 3. Given these observations, it is possible that step 1 involves a highly non-equilibrium mixture of phases undergoing transformation and, at larger distances, there is relaxation to  $\beta$ -Zr. It is also possible that step 1 has transformed fully to the  $\beta$ -phase (given the uncertainty bars in Figure 7) or large deviatoric stresses are present, which would serve to offset the stress from the Hugoniot. At steps 4-6, the stress-volume paths are similar, with each crossing the  $\alpha$ -Zr Hugoniot at  $\sim 16$  GPa and all terminal states falling near the  $\beta$ -Zr Hugoniot at 24 to 27 GPa. The inferred transformation parameters for the 2.0 mJ data are reported in Table 2 and a graphical representation is shown in Figure 8.

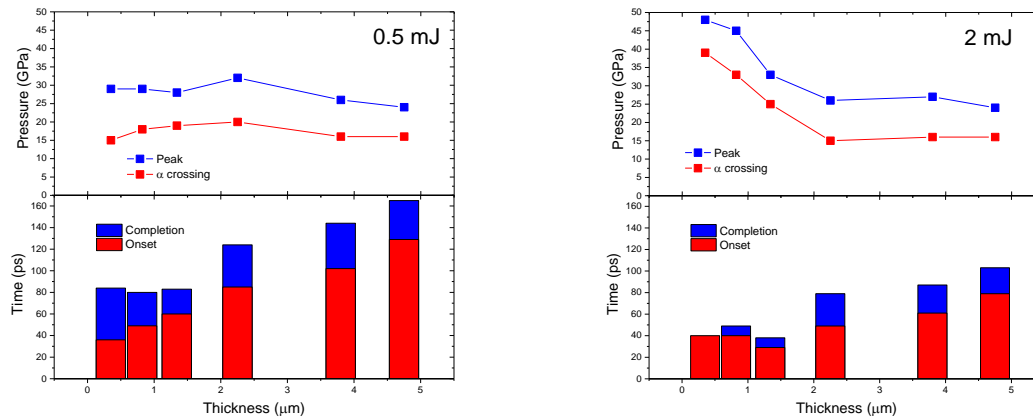
The equilibrium multi-phase Zr Hugoniot curve, which is derived from experimental measurements (on longer time scales) and the Greeff EOS, indicates the onset of the  $\omega$ - $\beta$  transition at a shock pressure of  $\sim 24$  GPa and completion at  $\sim 29$  GPa. In contrast, the data reported here suggest the onset of  $\alpha$ -Zr depletion at 15 to 20 GPa, with no clear signatures or evidence of  $\omega$ -Zr. This excludes the data at steps 1 and 2 in the 2.0 mJ data, given the presence of large overshoots in the velocity profiles. As discussed in the literature<sup>6</sup>, a kinetic limitation on the transformation to  $\omega$ -Zr would place the intersection of the shock Hugoniot with the metastable  $\alpha$ - $\beta$  phase boundary at approximately 13 to 18 GPa. As such, the data presented here appear to support the existence of an intermediate  $\beta$ -phase that is visited at  $\sim 15$  GPa, which would transform to  $\omega$ -Zr on longer time scales. Alternatively, the loading paths may involve the production of  $\omega$ -Zr and our analysis technique simply cannot detect it.

Table 1: Data from analysis of 0.5 mJ shots

<b>Step</b>	<b>1</b>	<b>2</b>	<b>3</b>	<b>4</b>	<b>5</b>	<b>6</b>
Peak stress (GPa)	29	29	28	32	26	24
Stress at $\alpha$ -Zr Hugoniot crossing (GPa)	15	18	19	20	16	16
Transformation onset time (ps)	36	49	60	85	102	129
Transformation completion time (ps)	84	80	83	124	144	165

Table 2: Data from analysis of 2.0 mJ shots

<b>Step</b>	<b>1</b>	<b>2</b>	<b>3</b>	<b>4</b>	<b>5</b>	<b>6</b>
Peak stress (GPa)	48	45	33	26	27	24
Stress at $\alpha$ -Zr Hugoniot crossing (GPa)	39	33	25	15	16	16
Transformation onset time (ps)	40	40	29	49	61	79
Transformation completion time (ps)	n/a	49	38	79	87	103



**Figure 8: Data from Lagrangian analysis of Zr shock compression shots at 0.5 mJ (left) and 2.0 mJ (right). Plotted here for each step thickness are the peak stress, the stress at the  $\alpha$ -Zr Hugoniot crossing, and estimates of the transformation onset and completion times.**

## Conclusions

Analysis of velocimetry data from thin layers of Zr shock-compressed to  $\sim 30$  and  $\sim 50$  GPa on an ultrafast time scale ( $< 1$  ns) indicates transformation from the  $\alpha$ -phase beginning in less than  $\sim 100$  ps. In all cases except the thinnest layers, the computed stress-volume paths terminate on the  $\beta$ -Zr Hugoniot. Even with conservative uncertainty estimates, the data analysis indicates significant production of  $\beta$ -Zr in less than  $\sim 200$  ps (during compression). We do not find any clear evidence of  $\omega$ -Zr, although we cannot rule it out. As a result, it seems reasonable to hypothesize a direct  $\alpha$ - $\beta$  transition under these loading conditions, with metastable  $\beta$  occurring as an intermediate at early times, potentially transforming to  $\omega$  at longer times scales (not probed here). Bypassing the  $\omega$ -phase with short drives (on the order of 100 ps) would be consistent with previous measurements<sup>6</sup> probing similar loading conditions using time-resolved x-ray diffraction (XRD).

Clear visual signatures of phase transformation, such as a distinct P1/P2 wave structure that is commonly observed at larger time and length scales, was not observed in our free-surface velocity measurements. Rather, it was necessary to employ a Lagrangian analysis

method to reveal solid-solid phase transitions. The lack of P1/P2 wave structure is likely due to transient states at short run distances (early times), with larger run distances needed to establish clear P1/P2 wave structure. Similar behavior was noted in ultrafast compression experiments performed on Fe, which probed the  $\alpha$ - $\epsilon$  transition on a similar time scale (hundreds of ps)<sup>1</sup>.

The approach adopted here, which involves a table-top ultrafast shock compression system combined with Lagrangian analysis, serves to complement dynamic compression measurements with time-resolved XRD. Ultrafast velocimetry enables the determination of stress-strain states at short time scales, a capability that is usually not available at high-flux x-ray facilities with sub-100-ps drive pulses. Taken together, the results from previous XRD work<sup>6</sup> and the current work provide detailed information on the thermodynamic paths and kinetic parameters of solid-solid phase transitions in shock-compressed Zr on a sub-nanosecond time scale.

### **Acknowledgements**

This work was performed under the auspices of the U.S. Department of Energy by Lawrence Livermore National Laboratory under Contract DE-AC52-07NA27344 (internal references: LDRD number 16-ERD-037 and LLNL-JRNL-829177). The authors thank Dr. Elis Stavrou and Dr. Art Nelson for the sample characterization data.

## References

- (1) Crowhurst, J. C.; Reed, B. W.; Armstrong, M. R.; Radousky, H. B.; Carter, J. A.; Swift, D. C.; Zaug, J. M.; Minich, R. W.; Teslich, N. E.; Kumar, M. The  $\alpha \rightarrow \epsilon$  Phase Transition in Iron at Strain Rates up to Similar to  $\sim 10^9 \text{ s}^{-1}$ . *J. Appl. Phys.* **2014**, *115* (11), 113506. <https://doi.org/10.1063/1.4868676>.
- (2) Greeff, C. W. Phase Changes and the Equation of State of Zr. *Model. Simul. Mater. Sci. Eng.* **2005**, *13* (7), 1015. <https://doi.org/10.1088/0965-0393/13/7/001>.
- (3) Cerreta, E.; Gray III, G. T.; Hixson, R. S.; Rigg, P. A.; Brown, D. W. The Influence of Interstitial Oxygen and Peak Pressure on the Shock Loading Behavior of Zirconium. *Acta Mater.* **2005**, *53* (6), 1751–1758. <https://doi.org/10.1016/j.actamat.2004.12.024>.
- (4) Rigg, P. A.; Greeff, C. W.; Knudson, M. D.; Gray, G. T. Influence of Impurities on the Solid-solid Phase Transitions in Zirconium. *AIP Conf. Proc.* **2009**, *1195* (1), 1171–1174. <https://doi.org/10.1063/1.3295010>.
- (5) Banerjee, S.; Mukhopadhyay, P. *Phase Transformations: Examples from Titanium and Zirconium Alloys*; Elsevier, 2010.
- (6) Armstrong, M. R.; Radousky, H. B.; Austin, R. A.; Stavrou, E.; Zong, H.; Ackland, G. J.; Brown, S.; Crowhurst, J. C.; Gleason, A. E.; Granados, E.; Grivickas, P.; Holtgrewe, N.; Lee, H. J.; Li, T. T.; Lobanov, S.; McKeown, J. T.; Nagler, B.; Nam, I.; Nelson, A. J.; Prakapenka, V.; Prescher, C.; Roehling, J. D.; Teslich, N. E.; Walter, P.; Goncharov, A. F.; Belof, J. L. Observation of Fundamental Mechanisms in Compression-Induced Phase Transformations Using Ultrafast X-Ray Diffraction. *JOM* **2021**, *73*, 2185-2193. <https://doi.org/10.1007/s11837-020-04535-4>.
- (7) Radousky, H. B.; Armstrong, M. R.; Austin, R. A.; Stavrou, E.; Brown, S.; Chernov, A. A.; Gleason, A. E.; Granados, E.; Grivickas, P.; Holtgrewe, N.; Lee, H. J.; Lobanov, S. S.; Nagler, B.; Nam, I.; Prakapenka, V.; Prescher, C.; Walter, P.; Goncharov, A. F.; Belof, J. L. Melting and Refreezing of Zirconium Observed Using Ultrafast X-Ray Diffraction. *Phys. Rev. Res.* **2020**, *2* (1), 013192. <https://doi.org/10.1103/PhysRevResearch.2.013192>.
- (8) Radousky, H. B.; Armstrong, M. R.; Goldman, N. Time Resolved X-Ray Diffraction in Shock Compressed Systems. *J. Appl. Phys.* **2021**, *129* (4), 040901. <https://doi.org/10.1063/5.0034929>.
- (9) Rigg, P. A.; Saavedra, R. A.; Scharff, R. J. Sound Speed Measurements in Zirconium Using the Front Surface Impact Technique. *J. Phys. Conf. Ser.* **2014**, *500* (3), 032014. <https://doi.org/10.1088/1742-6596/500/3/032014>.
- (10) Crowhurst, J. C.; Armstrong, M. R.; Knight, K. B.; Zaug, J. M.; Behymer, E. M. Invariance of the Dissipative Action at Ultrahigh Strain Rates Above the Strong Shock Threshold. *Phys. Rev. Lett.* **2011**, *107* (14), 144302. <https://doi.org/10.1103/PhysRevLett.107.144302>.
- (11) Crowhurst, J. C.; Armstrong, M. R.; Gates, S. D.; Zaug, J. M.; Radousky, H. B.; Teslich, N. E. Yielding of Tantalum at Strain Rates up to  $10^9 \text{ s}^{-1}$ . *Appl. Phys. Lett.* **2016**, *109* (9), 094102. <https://doi.org/10.1063/1.4960796>.
- (12) Moore, D. S. Shock Physics at the Nanoscale [Invited]. *JOSA B* **2018**, *35* (10), B1–B15. <https://doi.org/10.1364/JOSAB.35.0000B1>.
- (13) Reed, B. W.; Stolken, J. S.; Minich, R. W.; Kumar, M. A Unified Approach for Extracting Strength Information from Nonsimple Compression Waves. Part I: Thermodynamics and Numerical Implementation. *J. Appl. Phys.* **2011**, *110* (11), 113505. <https://doi.org/10.1063/1.3653821>.
- (14) Reed, B. W.; Reed Patterson, J.; Swift, D. C.; Stolken, J. S.; Minich, R. W.; Kumar, M. A Unified Approach for Extracting Strength Information from Nonsimple Compression

- Waves. Part II. Experiment and Comparison with Simulation. *J. Appl. Phys.* **2011**, *110* (11), 113506. <https://doi.org/doi:10.1063/1.3662173>.
- (15) Armstrong, M. R.; Crowhurst, J. C.; Bastea, S.; Zaug, J. M. Ultrafast Observation of Shocked States in a Precompressed Material. *J. Appl. Phys.* **2010**, *108* (2), 023511. <https://doi.org/10.1063/1.3460801>.
- (16) Steinberg, D. J. *Equation of State and Strength Properties of Selected Materials*; UCRL-MA-106439; Lawrence Livermore National Laboratory: UCRL-MA-106439: Livermore, CA, 1996.
- (17) Reed, B. W.; Patterson, J. R.; Nguyen, J. H.; Stölken, J. S.; Kumar, M. Bounds on the Rate-Dependent Plastic Flow of Tantalum up to 75 GPa. *J. Dyn. Behav. Mater.* **2021**, *7* (2), 307–324. <https://doi.org/10.1007/s40870-021-00296-6>.

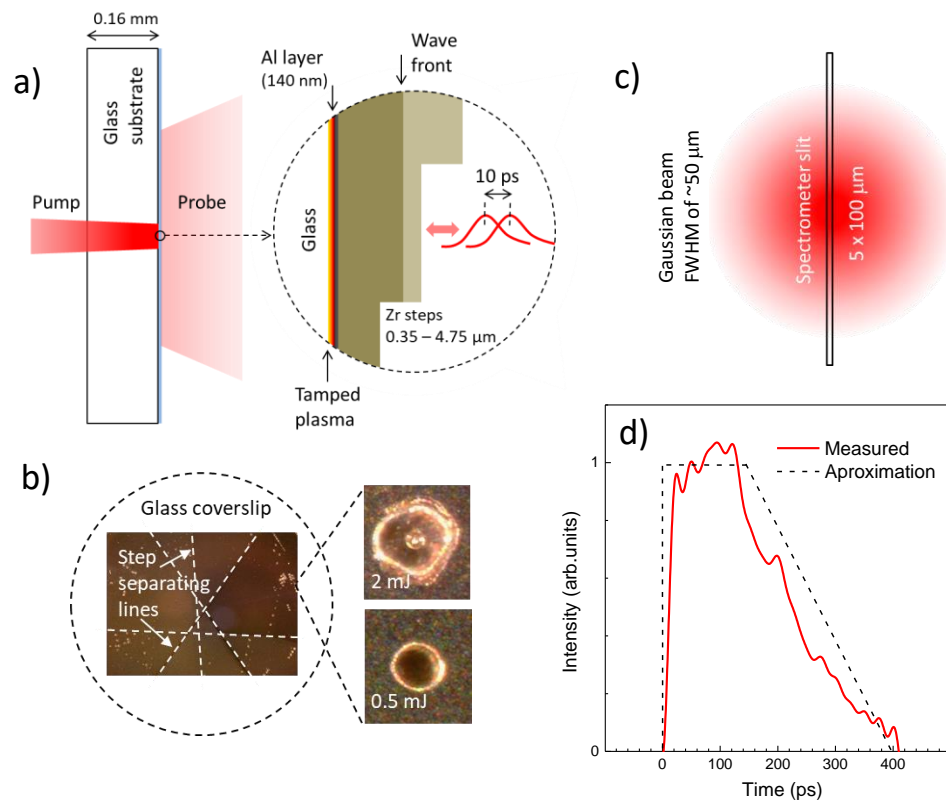


Fig. 1

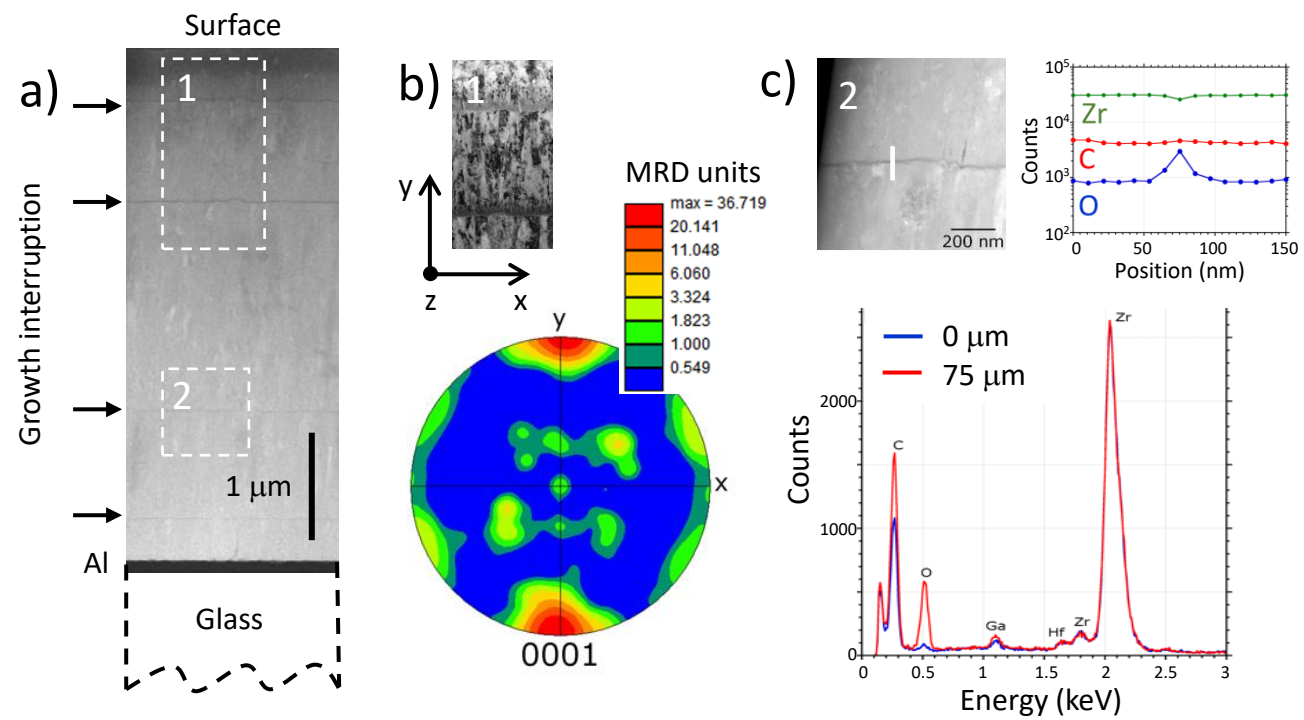


Fig. 2

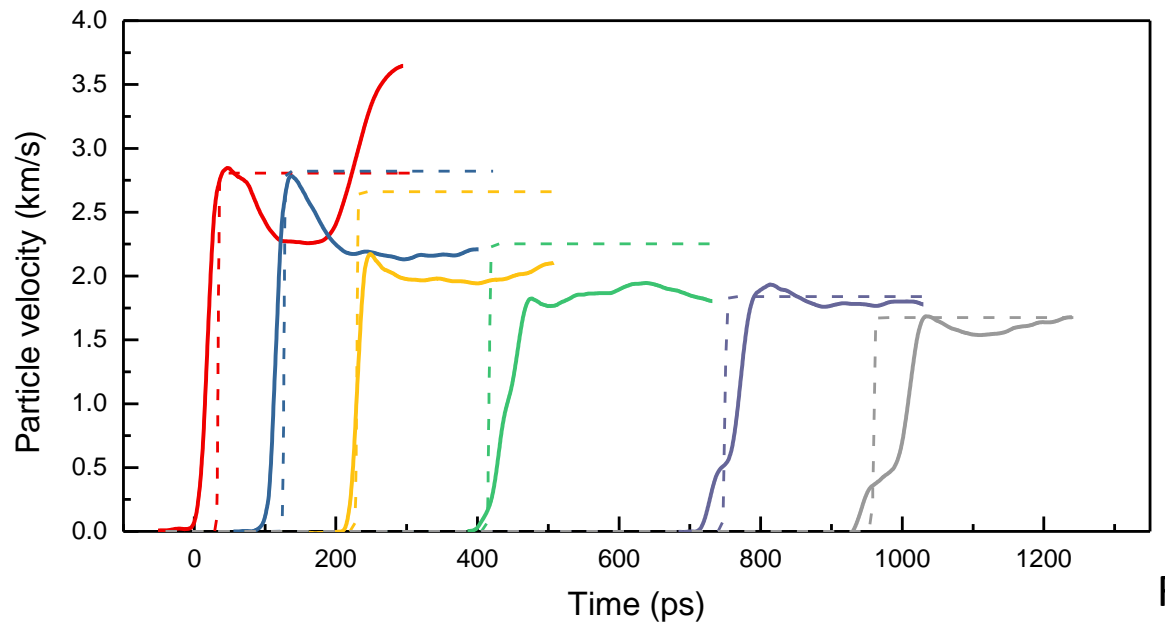
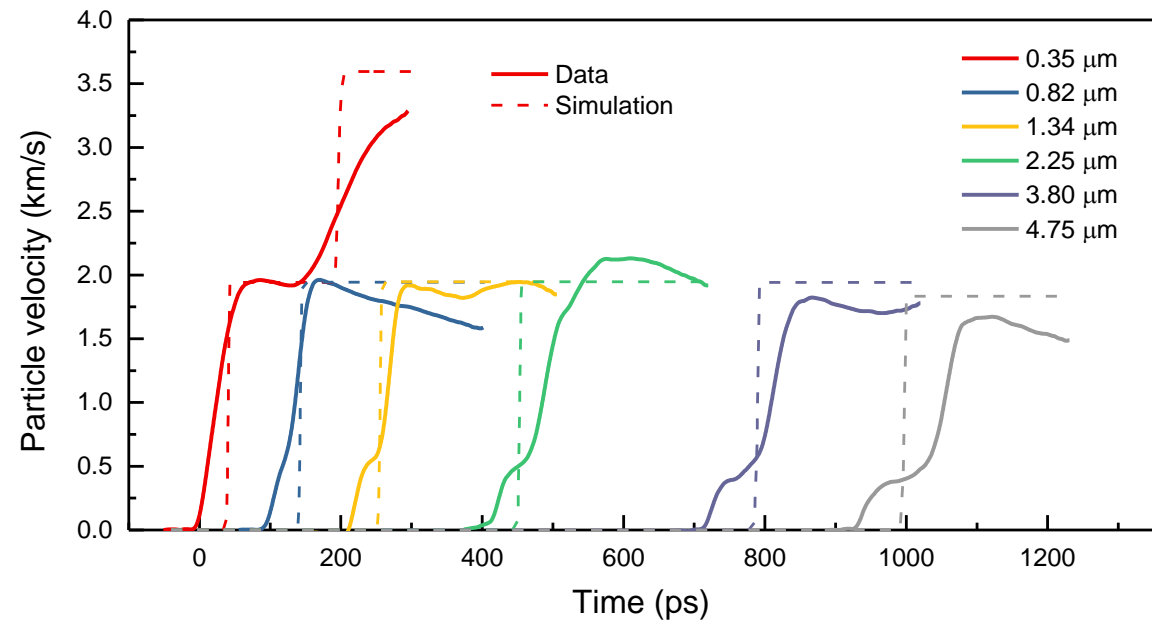
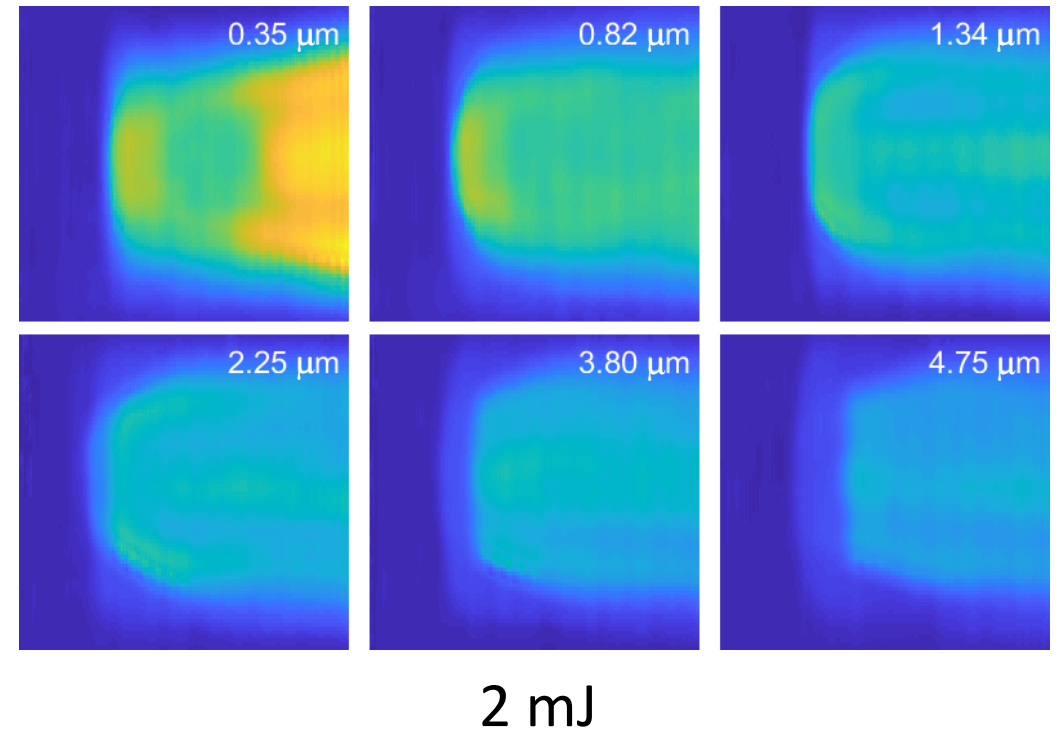
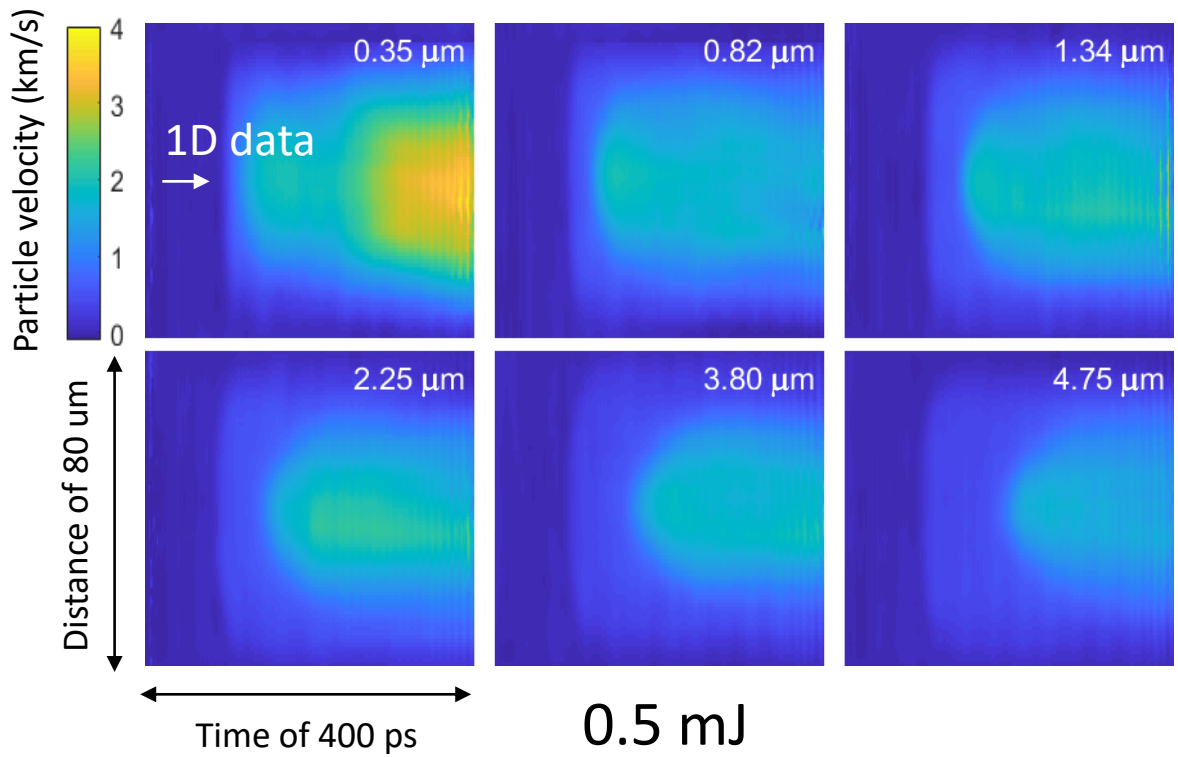


Fig. 3

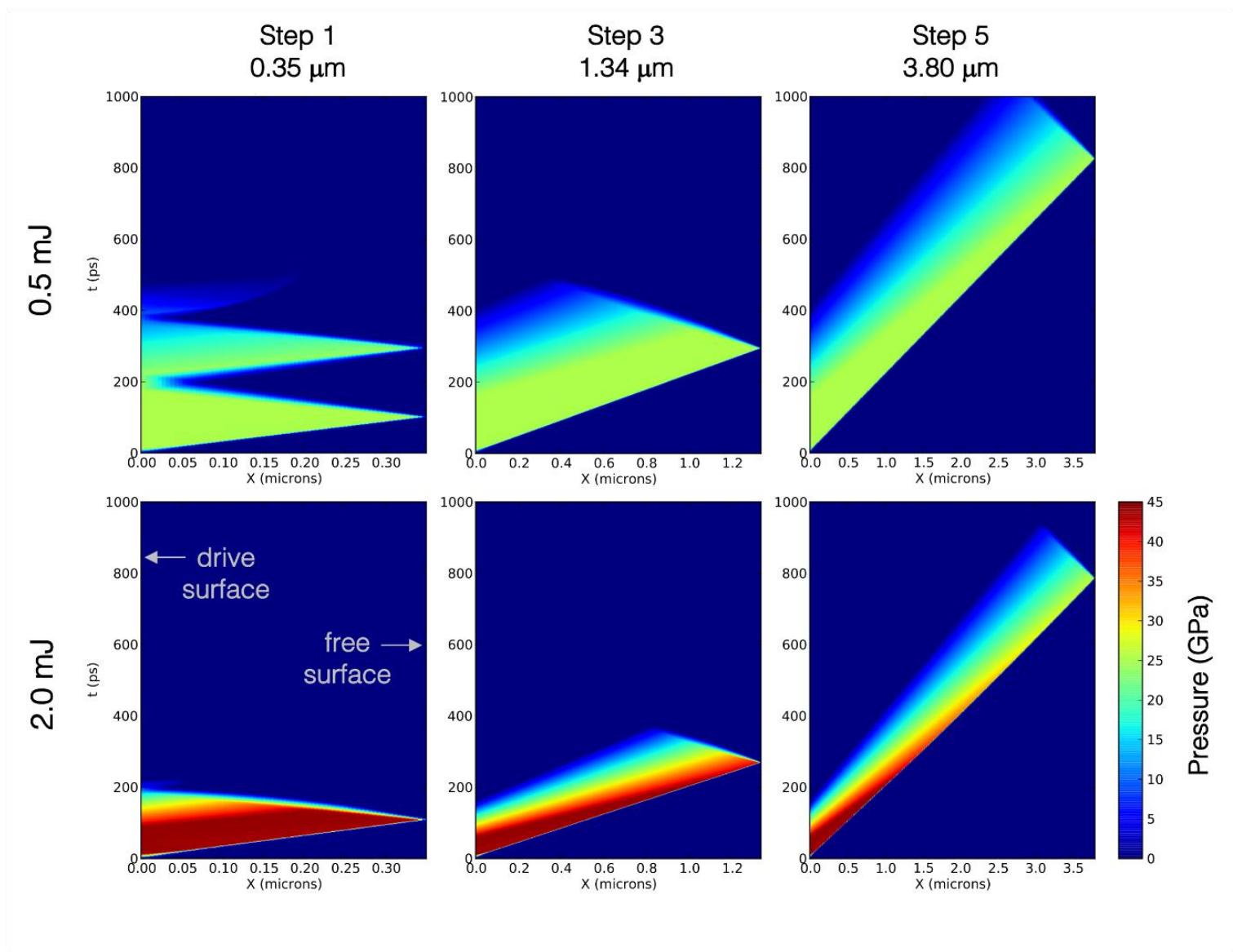


Fig. 4

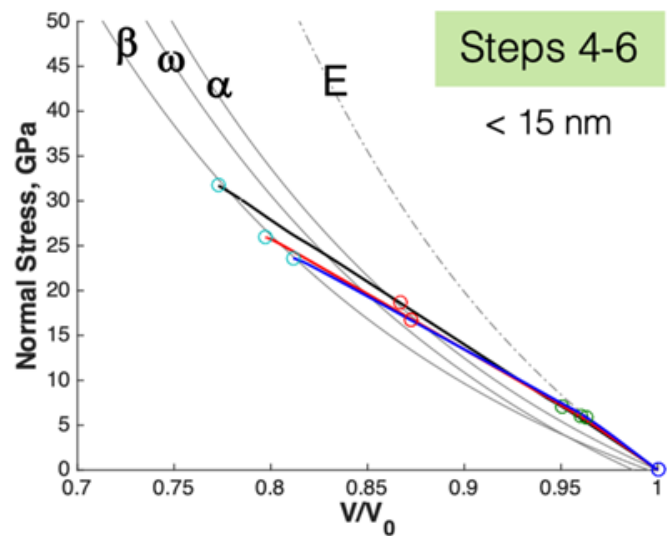
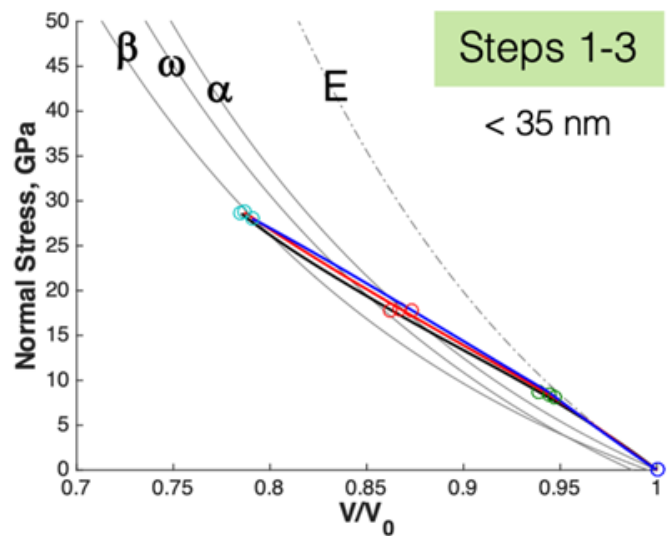
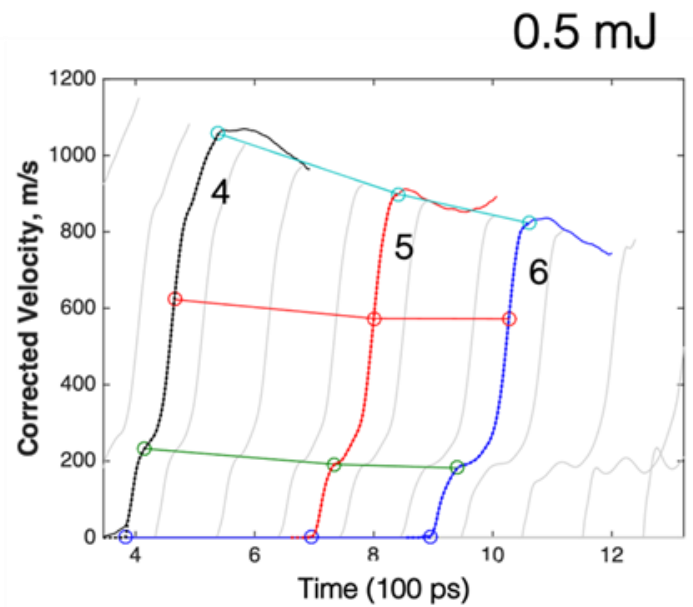
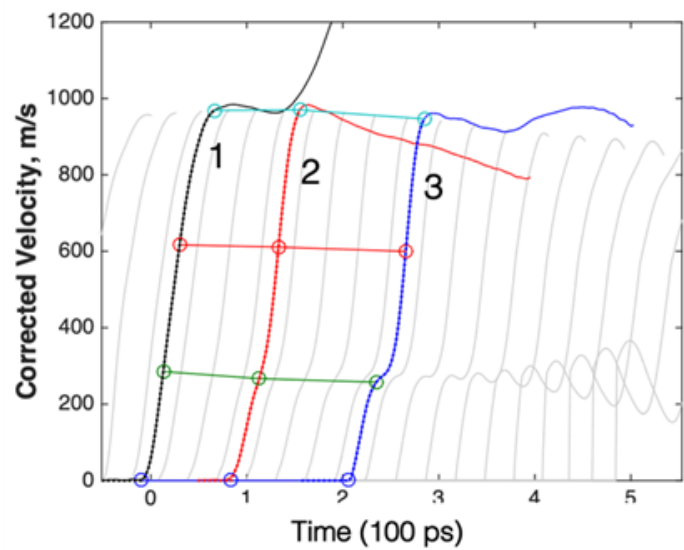


Fig. 5

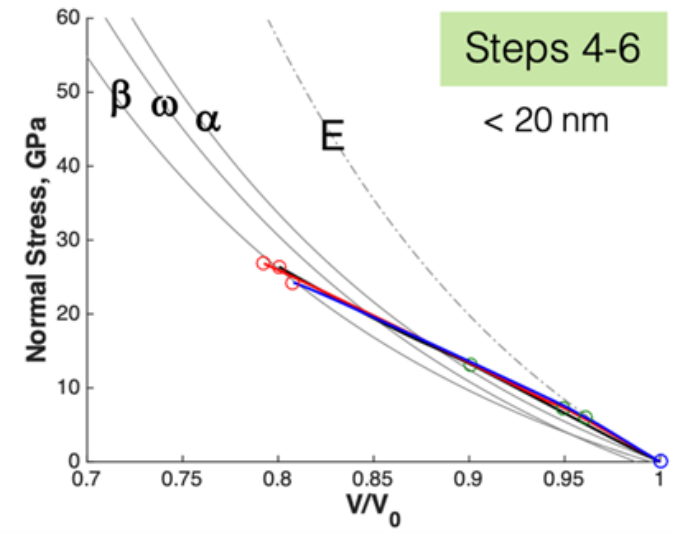
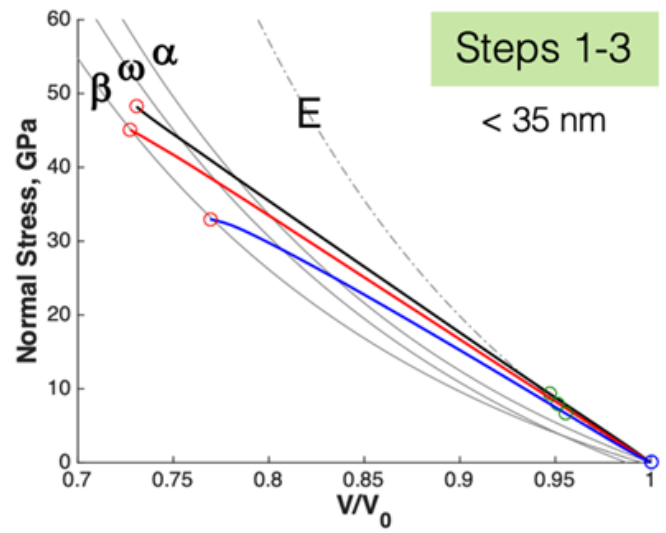
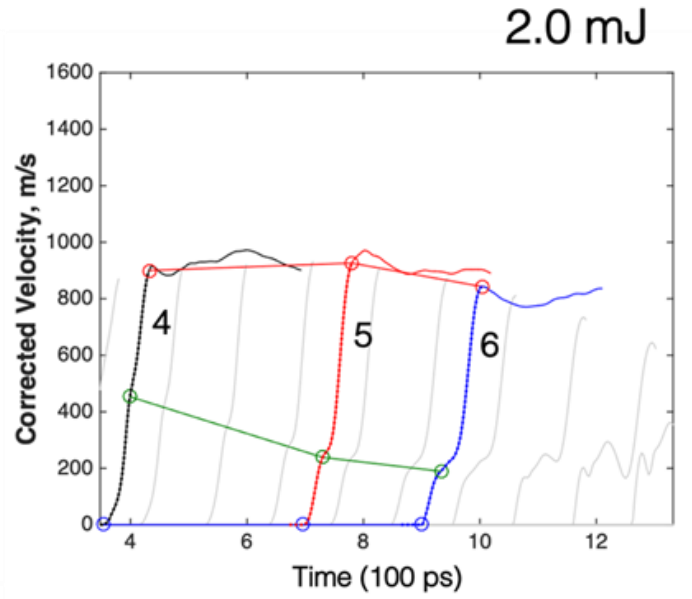
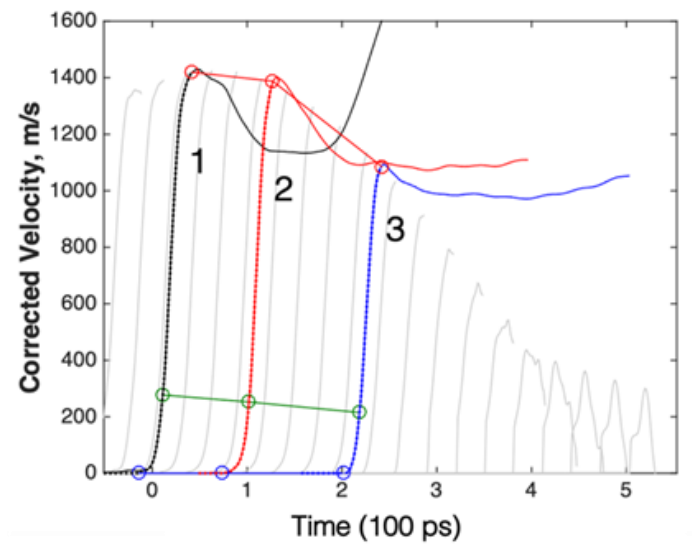


Fig. 6

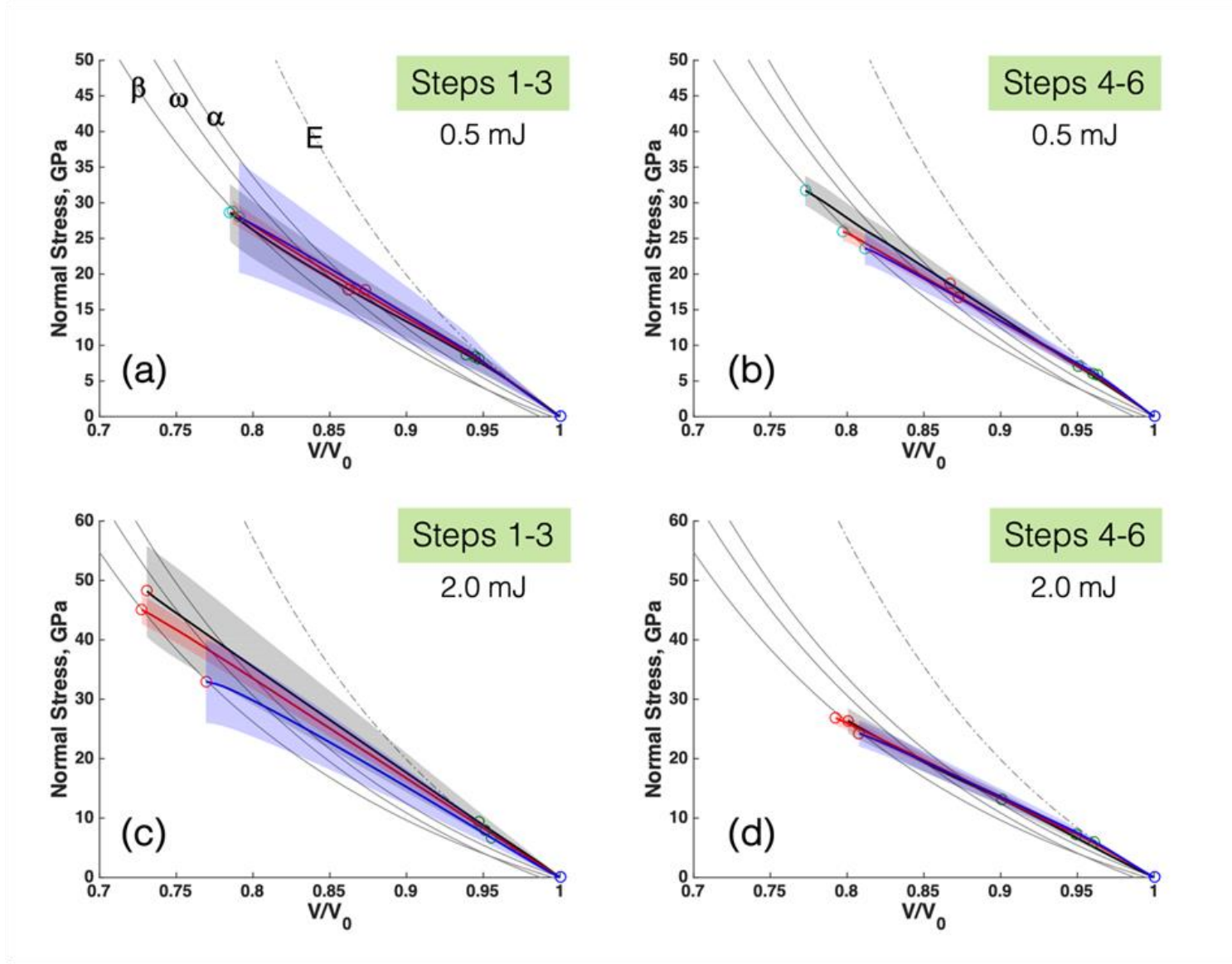


Fig. 7

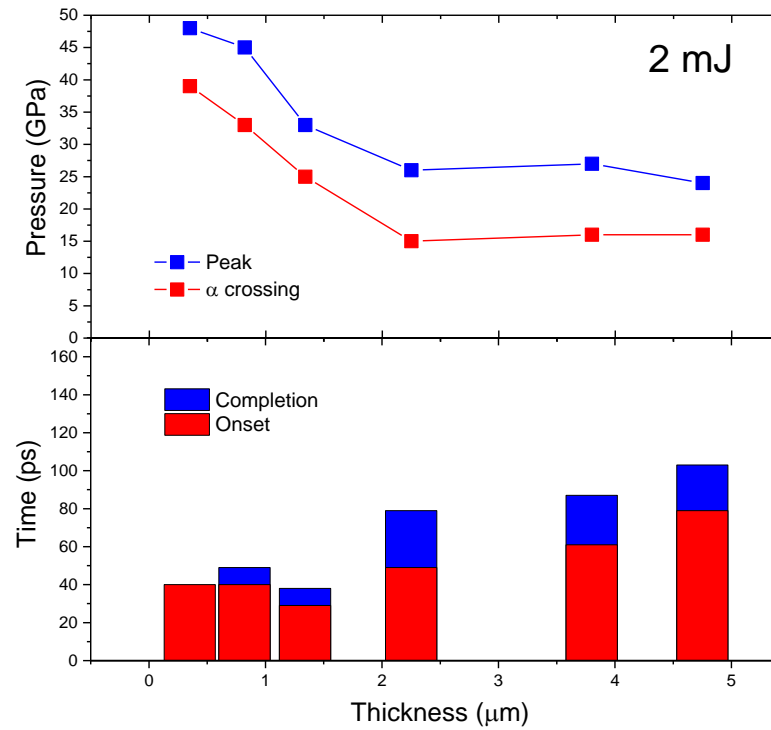


Fig. 8